Excited State Dynamics of a $CsPbBr_3$ Nanocrystal Terminated with Binary Ligands: Sparse Density of States with Giant Spin-Orbit Coupling Suppresses Carrier Cooling

SI Tables and Figures

Aaron Forde,[1] Talgat Inerbaev,[2,3,4] Erik Hobbie,[1] Dmitri Kilin[5]*

[1] *Department of Materials Science and Nanotechnology, North Dakota State University, Fargo, North Dakota 58102, United States*

[2] *Sobolev Institute of Geology and Mineralogy SB RAS, Novosibirsk*

[3] *National University of Science and Technology MISIS, 4 Leninskiy pr., Moscow 119049, Russian Federation*

[4] *L. N. Gumilyov Eurasian National University, Astana, Kazakhstan*

[5] *Department of Chemistry and Biochemistry, North Dakota State University, Fargo, North Dakota 58102, United States*

*Corresponding Author: dmitri.kilin@ndsu.edu

EXPERIMENTAL METHODS

Synthesis

Synthesis and isolation of $CsPbBr_3$ NCs follows a slightly modified protocol from Protesescu et. al.[1]

Materials: Cesium Carbonate (Cs_2CO_3, Aldrich 99.9 %), Oleic Acid (OA, Aldrich 90 %), Oleylamine (OAm, 90 %), Lead Bromide ($PbBr_2$, Aldrich 99.9 %), Octadecene (ODE, 90 %)

Preparation of Cs-Oleate: 0.41 g of Cs_2CO_3 was loaded into a 50 mL 3-neck flask with 20 mL ODE and 1.125 mL OA and heated to 100 C for 1 hour and then heated to 150 C under N_2 for 30 min to allow all precursors to react. When cooled to RT the Cs-Oleate separates into a gel-like phase.

Synthesis of $CsPbBr_3$ NCs: 10 mL ODE and 0.140 g of $PbBr_2$ were placed in a 50 mL 3-neck flask and heated to 120 C for 1 hour under vacuum. The flask was then put under an N_2 atmosphere and 1 ml OA and 1 ml OAm were injected to solubilize the precursors. Then the temperature was increased to 140 C and 0.8 mL of Cs-Oleate (heated to 120 C) was injected to produce NCs. Within 10 sec the 3-neck flask was placed in an ice bath.

Isolation of $CsPbBr_3$ NCs: The resultant product was centrifuged at 15000 rpm for 5 min to pellet the NCs out of ODE. The supernatant was discarded and the NCs were dispersed in dried toluene and bath sonicated for 5 min. The NCs in toluene where centrifuged again at 15000 rpm for 5 min to separate large aggregates. The supernatant was collected and the pellet discarded.

Optical Measurements

Absorption spectra of $CsPbBr_3$ NCs where collected using a 200 W tungsten bulb as a broad spectrum radiation source, which was then transmitted through the colloidal NC suspension

using optical fibers and recorded on an Ocean Optics spectrometer. The excitation also passed through a blank solvent (toluene) reference sample of the same volume as the colloidal suspension and the absorption spectrum was extracted using Beers law. PL was measured with a 375 nm laser in an integrating sphere using an Ocean Optics spectrometer

COMPUTATIONAL METHODS

Here we introduce the basic equations and quantities needed to define relevant observables and keep consistent notations in noncollinear spin DFT calculations.

$$\sum_{\sigma,\sigma' = \alpha,\beta}(- \delta_{\sigma\sigma'}\nabla^2 + v_{\sigma\sigma'}^{eff}(\vec{r}))\varphi_{i\sigma}(\vec{r}) = \varepsilon_{i,\sigma\sigma'}\,\varphi_{i\sigma'}(\vec{r}) \quad (1)$$

$$v_{\sigma\sigma'}^{eff}(\vec{r}) = \begin{pmatrix} v_{\alpha\alpha}^{eff}(\vec{r}) & v_{\alpha\beta}^{eff}(\vec{r}) \\ v_{\beta\alpha}^{eff}(\vec{r}) & v_{\beta\beta}^{eff}(\vec{r}) \end{pmatrix} \quad (2)$$

For equations (1)-(2), $\delta_{\sigma\sigma'}$ is the Kroenecker-delta function, σ and σ'define spin projections α or β, $v_{\sigma\sigma'}^{\text{eff}}(\vec{\text{r}})$ is the spin-dependent external potential, and $\varphi_{i\sigma}(\vec{r})$ is a spin-dependent KSO. The solution to the set of noncollinear spin DFT equations is represented as a superposition of spin- α and spin- β states $|\alpha\rangle = \begin{bmatrix}1\\0\end{bmatrix}$ and $|\beta\rangle = \begin{bmatrix}0\\1\end{bmatrix}$ with spatially dependent coefficents $\varphi_{i\alpha}(\vec{r})$ and $\varphi_{i\beta}$ $(\vec{r})$. These solutions are commonly referred to as spinor KSOs (SKSOs) shown in equation (3).

$$\varphi_i^{SKSO}(\vec{r}) = \begin{Bmatrix} \varphi_{i\alpha}(\vec{r}) \\ \varphi_{i\beta}(\vec{r}) \end{Bmatrix} = \varphi_{i\alpha}(\vec{r})|\alpha\rangle + \varphi_{i\beta}(\vec{r})|\beta\rangle \quad (3)$$

SKSOs obey normalization, equation (4), and orthogonality, equation (5)

$$\int d\vec{r}\begin{Bmatrix}\varphi_{i\alpha}^* & \varphi_{i\beta}^*\end{Bmatrix}\begin{Bmatrix}\varphi_{i\alpha} \\ \varphi_{i\beta}\end{Bmatrix} = \int d\vec{r}\left(\varphi_{i\alpha}^*(\vec{r})\,\varphi_{i\alpha}(\vec{r}) + \varphi_{i\beta}^*(\vec{r})\,\varphi_{i\beta}(\vec{r})\right) = 1 \quad (4)$$

$$\int d\vec{r}\left(\varphi_{i\alpha}^*(\vec{r})\,\varphi_{j\alpha}(\vec{r}) + \varphi_{i\beta}^*(\vec{r})\,\varphi_{j\beta}(\vec{r})\right) = \delta_{ij} \quad (5)$$

Within the noncollinear spin DFT framework, relativistic effects can be incorporated using scalar relativistic corrections.

$$H^{\text{relativistic}} = H^{SR} + H^{SOC} \quad (6)$$

The relativistic Hamiltonian is composed of two terms: H^{SR} describes relativistic kinetic energy corrections and H^{SOC}describes the energy shifts of spin occupations due to coupling with orbital angular momentum. H^{SOC} can be represented as

$$H^{SOC} = \frac{\hbar}{4m^2c^2r}\frac{1\partial v_{\text{sphere}}^{KS}}{\partial r}\vec{L}\cdot\vec{S} \tag{7}$$

where $\vec{L}$ is the angular momentum operator and $\vec{S}$ is composed of Pauli spin matrices ($\hat{\sigma}_x$, $\hat{\sigma}_y$, $\hat{\sigma}_z$).

The magnetization vector $\vec{M} = [M_x, M_y, M_z]$ in noncollinear spin DFT is constructed from the SKSO density matrix $\hat{\rho}^{NCS}(\vec{r}) = \begin{pmatrix}\rho_{\alpha\alpha}(\vec{r}) & \rho_{\alpha\beta}(\vec{r})\\ \rho_{\beta\alpha}(\vec{r}) & \rho_{\beta\beta}(\vec{r})\end{pmatrix}$. Components within the density matrix are found from $\rho_{\sigma,\sigma'}(\vec{r}) = \sum_{\sigma,\sigma'} f_i^{NCS}\varphi_{i\sigma}^{NCS}(\vec{r})\,\varphi_{i\sigma'}^{NCS}(\vec{r})$, where f_i^{NCS} is the occupation number of the *i*th SKSO and takes values between 0 and 1. Magnetization density projections $m_i(\vec{r})$ are found from expectation values of the corresponding Pauli matrices $\hat{\sigma}_i$, i=x, y, z, shown in equations (8a)-(8e)[2].

$$\rho_{Tr}(\vec{r}) = Tr(\hat{\rho}^{NCS}(\vec{r})) = \rho_{\alpha\alpha}(\vec{r}) + \rho_{\beta\beta}(\vec{r}) \tag{8a}$$

$$m_x(\vec{r}) = \mu_B Tr(\hat{\rho}^{NCS}(\vec{r})\hat{\sigma}_x) = \mu_B(\rho_{\alpha\beta}(\vec{r}) + \rho_{\beta\alpha}(\vec{r})) \tag{8b}$$

$$m_y(\vec{r}) = -i\mu_B Tr(\hat{\rho}^{NCS}(\vec{r})\hat{\sigma}_y) = -i\mu_B(\rho_{\alpha\beta}(\vec{r}) - \rho_{\beta\alpha}(\vec{r})) \tag{8c}$$

$$m_z(\vec{r}) = \mu_B Tr(\hat{\rho}^{NCS}(\vec{r})\hat{\sigma}_z) = \mu_B(\rho_{\alpha\alpha}(\vec{r}) - \rho_{\beta\beta}(\vec{r})) \tag{8d}$$

$$M_x = \int dr m_x(\vec{r}),\ M_y = \int dr m_y(\vec{r}),\ M_z = \int dr m_z(\vec{r}) \tag{8e}$$

Density of states for SKSOs are represented as $D_{SKSO} = \sum_i \delta(\varepsilon - \varepsilon_i^{SKSO})$ with the delta function being approximated as a Gaussian distribution.

A spin-restricted basis was used for adiabatic molecular dynamics. The total kinetic energy of the system is set equal to a thermostat, equation (9a), for an initial condition and is propagated by

using Newton's equations of motion, equation (9b). The energy of KSOs are recorded for each timestep to observe fluctuations in time, equation (9c).

$$\sum_{I=1}^{N^{ion}} \frac{M_I}{2}\left(\frac{d\vec{R}_I}{dt}\Big|_{t=0}\right)^2 = \frac{3}{2}N^{ion}k_B T \tag{9a}$$

$$\frac{d^2}{dt^2}\vec{R}_I = \vec{F}_I/M_I \tag{9b}$$

$$\varepsilon_i(t) = \varepsilon_i\left(\overrightarrow{R_I(t)}\right) \tag{9c}$$

NACs can be computed using the "on-the-fly" procedure along a nuclear trajectory

$$\hat{V}_{ij}^{NA}(t) = -\frac{i\hbar}{2\Delta t}\int d\vec{r}\left\{\varphi_{i\alpha}^*(\vec{r},\{\vec{R}_I(t)\}) \quad \varphi_{i\beta}^*(\vec{r},\{\vec{R}_I(t)\})\right\}\cdot\begin{Bmatrix}\varphi_{j\alpha}\left(\vec{r},\{\vec{R}_I(t+\Delta t)\}\right)\\ \varphi_{j\beta}\left(\vec{r},\{\vec{R}_I(t+\Delta t)\}\right)\end{Bmatrix} + h.c. \tag{10}$$

The Fourier transform of the autocorrelation function, equation (11a)-(11c), provides components of the Redfield tensor, equation (11d).

$$M_{ijkl}(\tau) = \frac{1}{T}\int_0^T V_{ij}^{NA}(t+\tau)V_{kl}^{NA}(t)dt \tag{11a}$$

$$\Gamma_{ijkl}^{+} = \frac{1}{T}\int_0^T M_{ijkl}(\tau)e^{-i\omega_{kl}\tau}d\tau \tag{11b}$$

$$\Gamma_{ijkl}^{-} = \frac{1}{T}\int_0^T M_{ijkl}(\tau)e^{-i\omega_{ij}\tau}d\tau \tag{11c}$$

$$R_{ijkl} = \Gamma_{ijkl}^{+} + \Gamma_{ijkl}^{-} + \delta_{lj}\sum_m \Gamma_{ijkl}^{+} - \delta_{ik}\sum_m \Gamma_{ijkl}^{-}, \tag{11d}$$

The Redfield tensor controls dissipative dynamics of the density matrix, equation (12).

$$\left(\frac{d\rho_{ij}}{dt}\right)_{diss} = \sum_{lm} R_{ijlm}\rho_{lm} \tag{12}$$

Diagonalizing the density matrix at each timestep along the excited state trajectory, we can compute time-resolved observables, such as changes in charge-carrier occupation relative to ground state charge density, equations (13a)-(13b), and average charge-carrier energy, equation (13c).

$$n^{(a,b)}(\varepsilon,t) = \sum_i \rho_{ii}^{(a,b)}(t)\delta(\varepsilon - \varepsilon_i) \tag{13a}$$

$$\Delta n^{(a,b)}(\varepsilon,t) = n^{(a,b)}(\varepsilon,t) - n^{eq}(\varepsilon,t) \quad (13b)$$

$$\langle \Delta\varepsilon_e \rangle(t) = \sum_{i \geq LU} \rho_{ii}(t)\varepsilon_i(t) \quad (13c)$$

From the average charge-carrier energy along excited-state trajectory we generate a dimensionless energy, eq 14

$$\langle E_e \rangle(t) = \frac{\langle \Delta\varepsilon_e \rangle(t) - \langle \Delta\varepsilon_e \rangle(\infty)}{\langle \Delta\varepsilon_e \rangle(0) - \langle \Delta\varepsilon_e \rangle(\infty)} \quad (14)$$

Along the excited-state trajectory, time-resolved PL can be computed between states *i* and *j* by using oscillator strength f_{ij} and is based on the concept of inverse population, equation (15a). Summing equation (15a) provides time-integrated emission, equation (15b).

$$E(\hbar\omega,t) = \sum_{j>i} f_{ij}\delta(\hbar\omega - \hbar\omega_{ij})\{\rho_{jj}(t) - \rho_{ii}(t)\} \quad (15a)$$

$$E^{tot}(\hbar\omega) = \frac{1}{T}\int_0^T E(\hbar\omega,t)dt \quad (15b)$$

SUPPLEMENTAL FIGURES AND TABLES

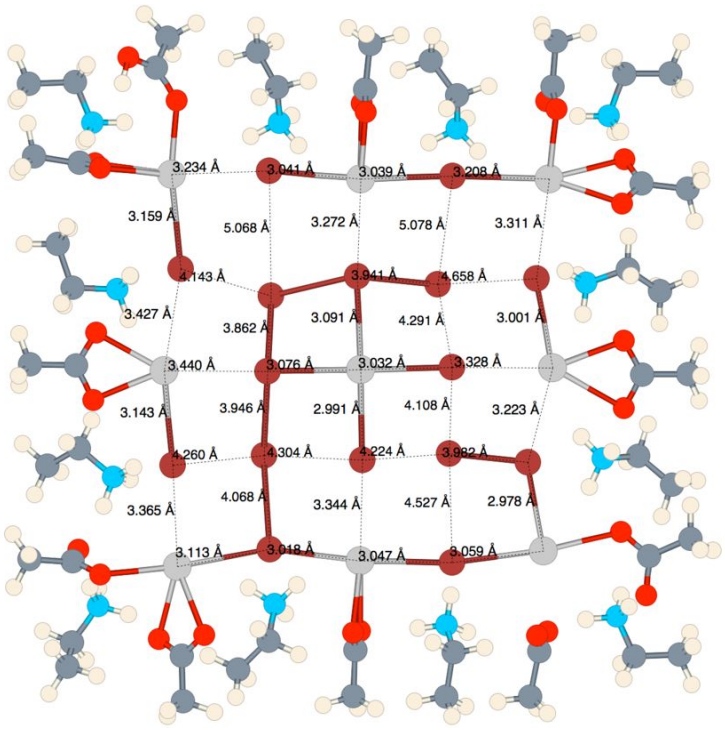

SI Figure S1: 2D projection of our atomistic $CsPbBr_3$ NC model which displays bond distances between Pb (grey) and Br (brown) ions.

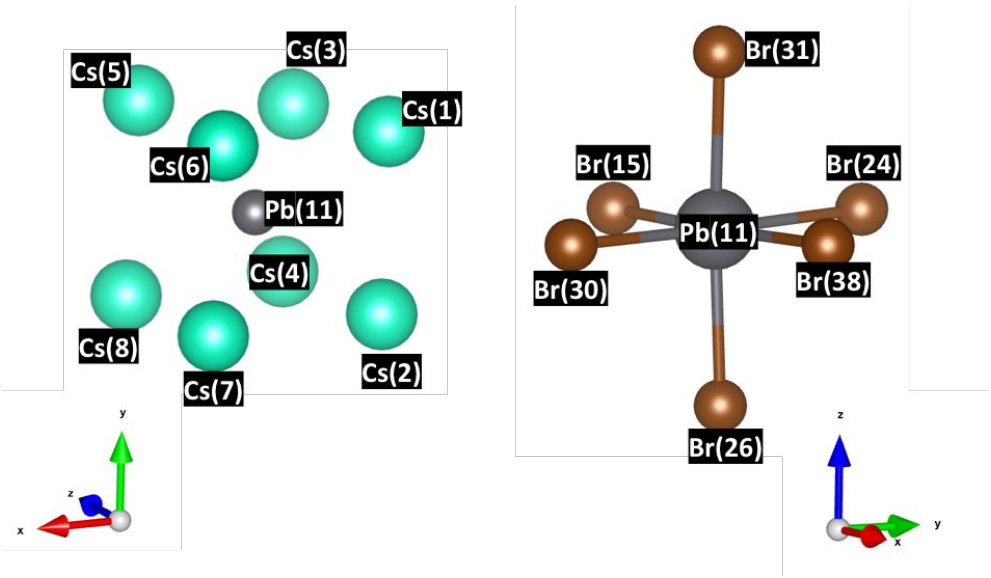

SI Figure S2: Orientation of Cs (blue) and Br (brown) ions around the central Pb atom within the NC. The labels correspond to SI Table S1 which displays bond distances and bond angles.

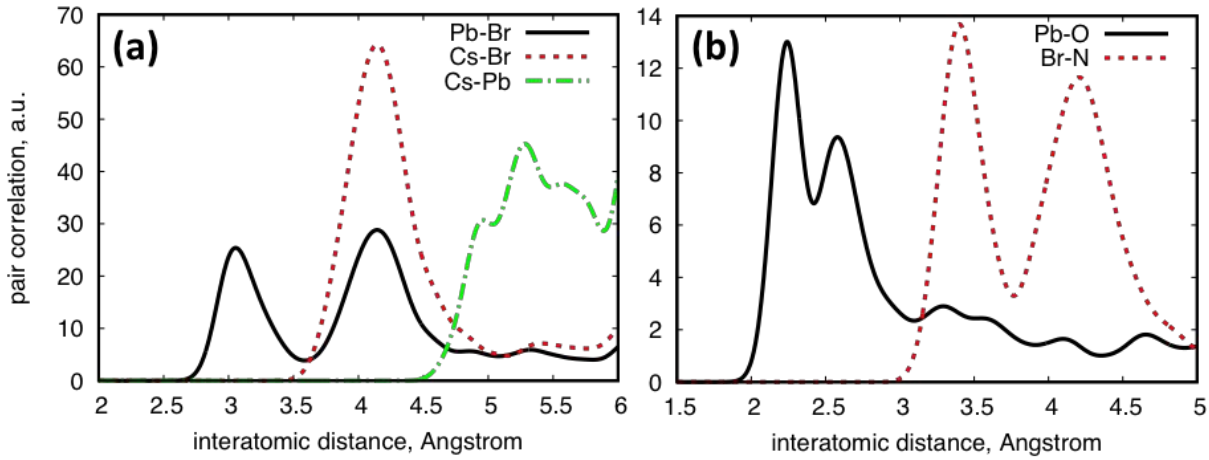

SI Figure S3: Radial distribution functions (RDFs) showing pair-wise distances between (a) inorganic atomic species and (b) functional groups of the passivating organic ligands. For the inorganic species we show distribution of Pb-Br bonds (black, solid), Cs-Br distances (red, dotted), and Cs-Pb distances (green, dash-dot). For the organic components, we show distribution of Pb-O bond distances (black, solid) and Br-N distances (red, dotted).

Br(x)-Pb(11)-Br(y)	Angle [degree]	Pb(11)-Br(x)	Distance [A]	Pb(11)-Cs(x)	Distance [A]
Br(31)-Pb(11)-Br(38)	84.95	Pb(11)-Br(38)	3.15	Pb(11)-Cs(1)	4.96
Br(24)-Pb(11)-Br(31)	89.41	Pb(11)-Br(31)	3.08	Pb(11)-Cs(2)	4.95
Br(15)-Pb(11)-Br(31)	93.43	Pb(11)-Br(30)	2.99	Pb(11)-Cs(3)	4.70
Br(30)-Pb(11)-Br(31)	89.81	Pb(11)-Br(26)	3.03	Pb(11)-Cs(4)	4.99
Br(30)-Pb(11)-Br(38)	92.64	Pb(11)-Br(15)	2.97	Pb(11)-Cs(5)	4.95
Br(26)-Pb(11)-Br(38)	89.50	Pb(11)-Br(24)	3.09	Pb(11)-Cs(6)	4.85
Br(24)-Pb(11)-Br(38)	88.49	x	x	Pb(11)-Cs(7)	4.88
Br(30)-Pb(11)-Br(26)	90.10	x	x	Pb(11)-Cs(8)	4.91
Br(30)-Pb(11)-Br(15)	89.30				
Br(26)-Pb(11)-Br(24)	90.80				
Br(26)-Pb(11)-Br(15)	92.13				
Br(24)-Pb(11)-Br(15)	89.55				

SI Table S1: Table of Pb-Br and Pb-Cs bond distances and Pb-Br bond angles which correspond to SI Figure S2

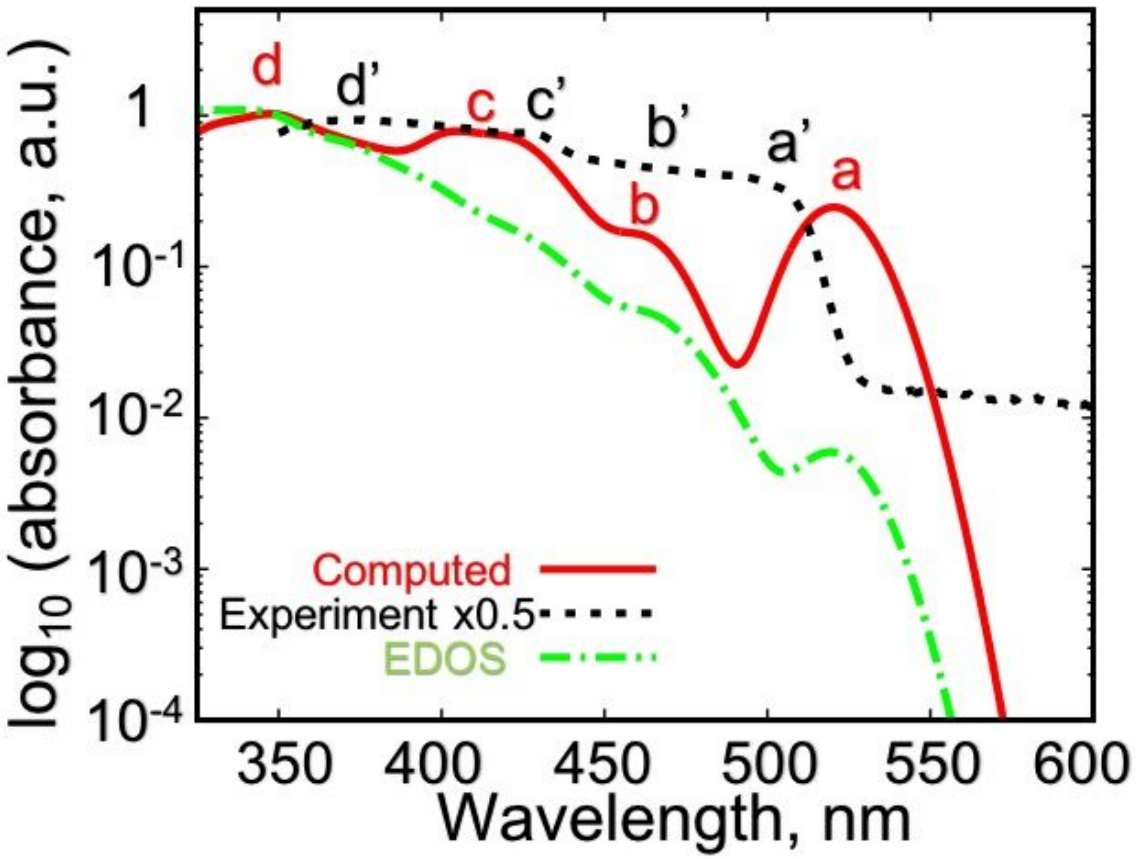

SI Figure S4: Same plot as **Figure 1(c)** but with absorption plotted in $\log_{10}$ scale. This allows a comparison of the relative intensities of computed spectra (red, solid), experimental spectra (black, dotted), and EDOS (green, dot-line) peaks. It is seen that the 'a' feature shows ~1.5 orders of magnitude higher intensity than the EDOS of the same transition energy. This indicates that even though the lowest energy transition has a low degeneracy, the intensity of the transition is very large. With increasing transition energy, the difference between relative intensities decreases. This is the expected trend for a particle in a box type system.

Transition Peaks in DOS			Peaks in Spectrum		
Notation	λ , nm	ΔE, eV	Notation	λ, nm	ΔE eV
$s_h \rightarrow s_e$	521	2.38		Computed	
$p_h \rightarrow s_e$	451	2.75	a	521	2.38
$d_h \rightarrow s_e$	441	2.81	b	464	2.67
$s_h \rightarrow d_e$	437	2.84	c	418	2.97
$p_h \rightarrow p_e$	432	2.87	d	355	3.49
$s_h \rightarrow p_e$	426	2.91		Experiment	
$d_h \rightarrow p_e$	423	2.93	a'	514	2.41
$p_h \rightarrow d_e$	418	2.97	b'	475	2.61
$d_h \rightarrow d_e$	360	3.44	c'	426	2.91
			d'	371	3.34

SI Table S2: Left side of the table corresponds to transitions types illustrated in **Figure 1(d)** based on the symmetry of the envelope function. Right side of the table corresponds to alphabetically labeled features in **Figure 1(c)** for computed and experimental spectra.

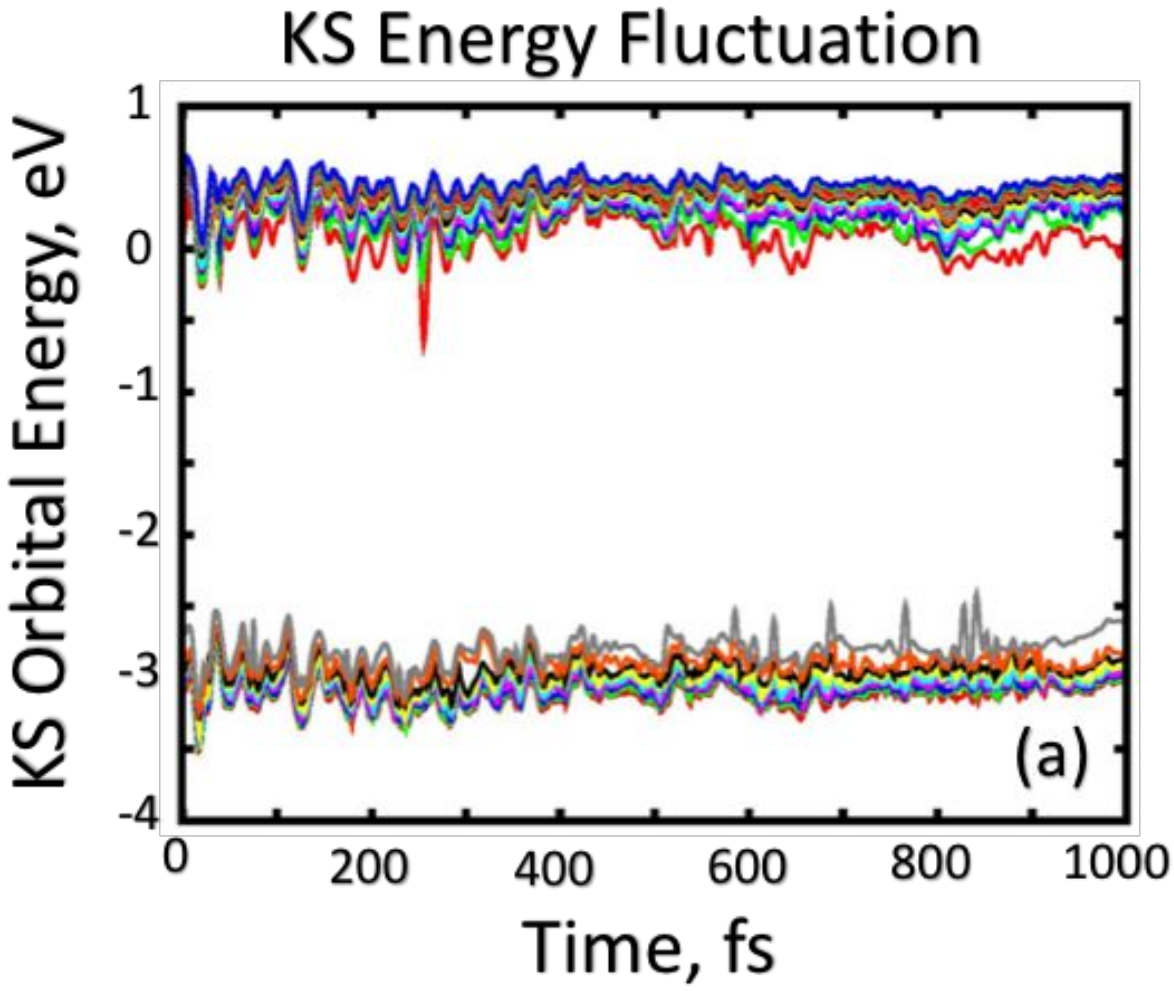

SI Figure S5*:* Energy fluctuations of adiabatic KSOs during molecular dynamics trajectory of 1 ps. Fluctuations in energy occur due to static coupling (diagonal elements of Born-Oppenheimer Hamiltonian) of electronic and nuclear degrees of freedom. Bottom/top half of the figure corresponds to a window of KSOs in the valence/conduction band from HO-x to HO/LU+y to LU.

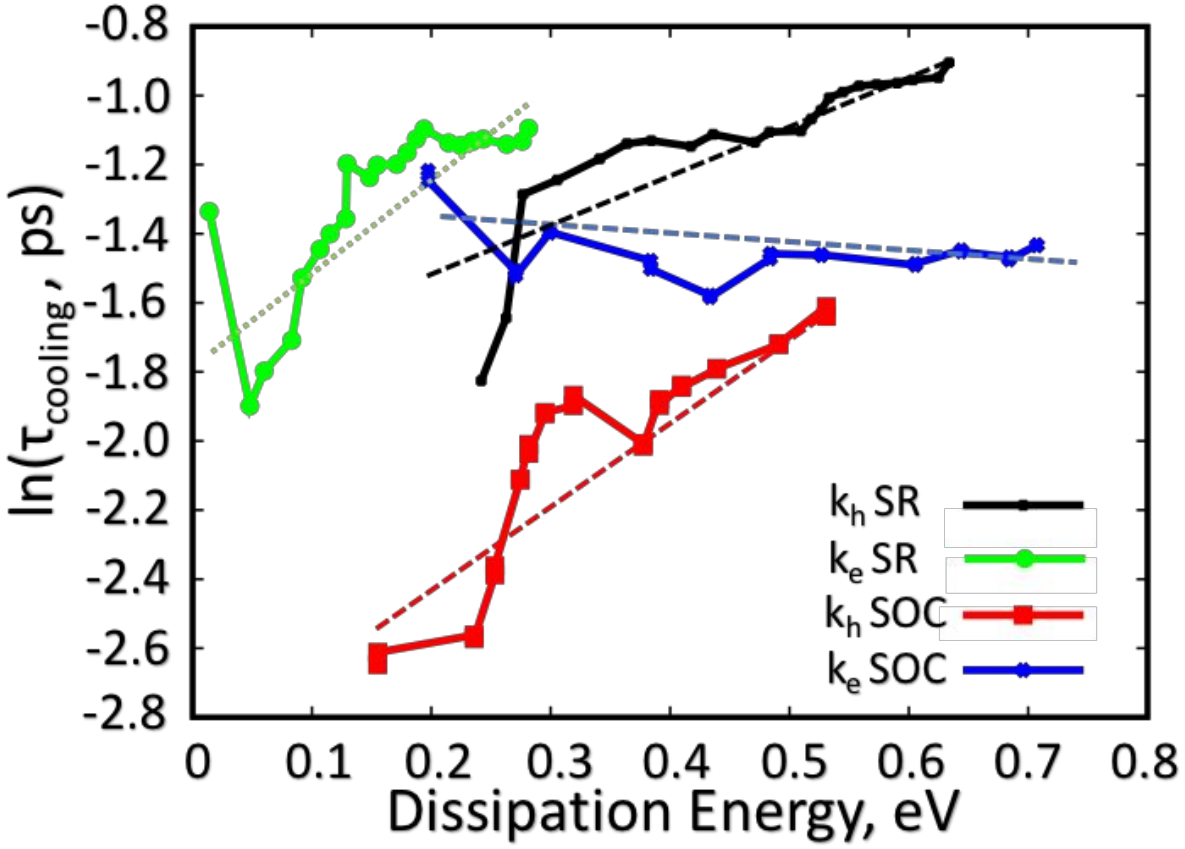

SI Figure S6*:* Illustrating trends in computed hot carrier cooling of charge carriers in $CsPbBr_3$ NCs using SR and spinor basis. Dotted lines represent a linear fit to each curve. Lowest energy transition corresponds to HO-1 → HO/LU+1→LU transitions. In SR basis, both hot electron (green, large dot) and hole (black, small dot) show trends roughly corresponding to the gap law, $\ln\{\tau_{cooling}\} \propto \Delta E_{dissipation}$. In the spinor basis, the hot hole (red, square) has the same main features as the SR-computed hot hole relaxation, while the hot electron (blue, cross) displays a constant carrier relaxation time independent of excitation energy. The constant hot electron relaxation time can be attributed to strong SOC interaction in the conduction band of $CsPbBr_3$ NC (see discussion for more detail).

$\ln(\tau_e)_{SOC} - \ln(\tau_e)_{SR}$	$\ln(\tau_h)_{SOC} - \ln(\tau_h)_{SR}$
$-2.64\Delta E + 0.33$	$1.03\Delta E - 1.06$

SI Table S3: We take the linear fit curves for each charge carrier (electron, hole) and subtract the linear curve for the SR computed data from the SKSO. The slope of the resultant equation represents the degree to which intraband cooling rates differ between the SKSO and SR methodologies. The constant represents differences between lowest energy intraband transition rate and lowest transition energy. It is seen that there is larger variation in the hot-electron cooling rates than in the hot-hole cooling rates. This indicates that SOC has larger impact for electron cooling than hole cooling.

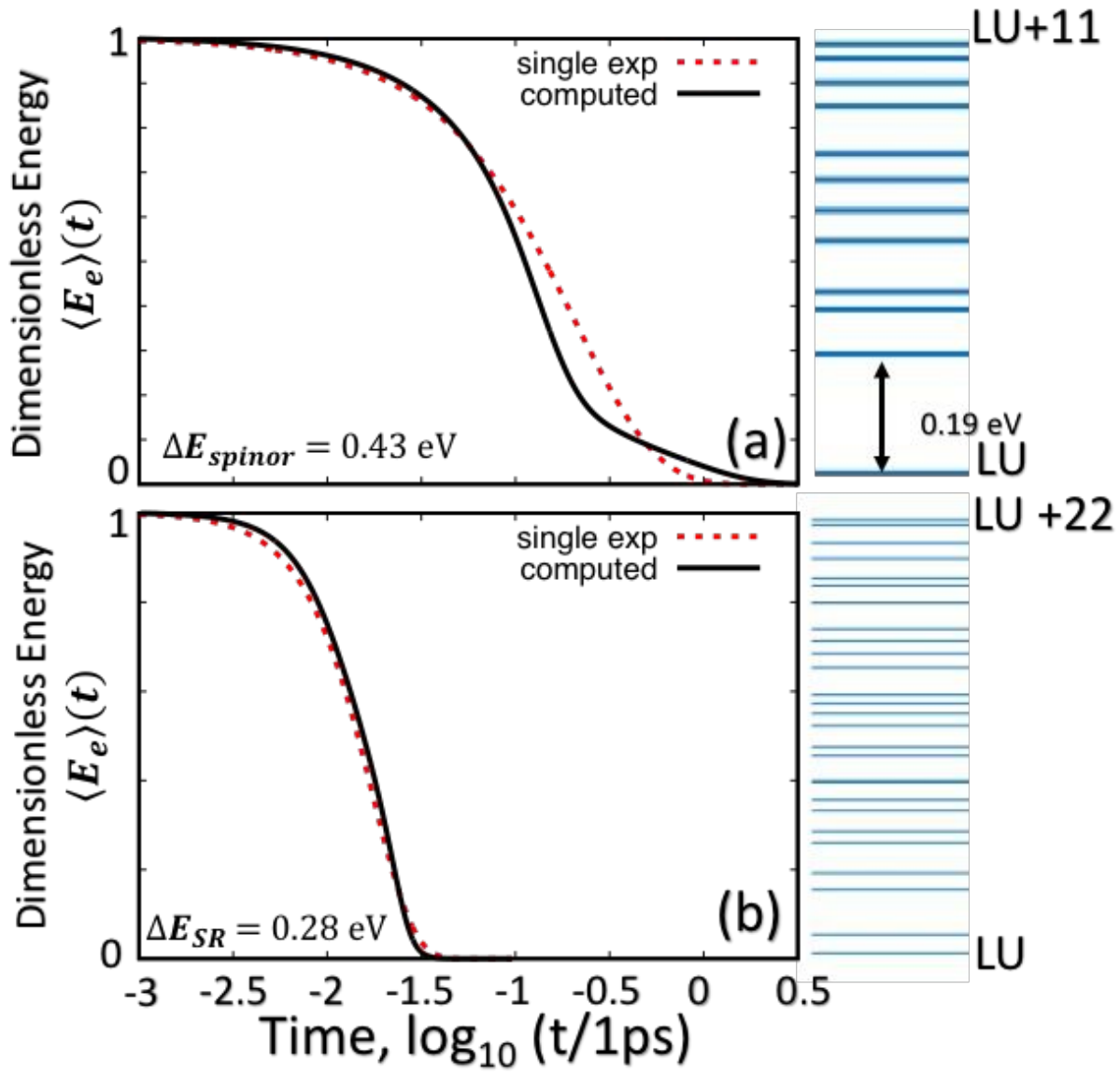

SI Figure S7*:* Hot electron cooling along excited-state trajectory using **(a)** spinor basis and **(b)** SR basis. The dissipation energy is normalized to a dimensionless energy $\langle E_e \rangle(t)$. In each panel the computed hot electron cooling (black, solid) is compared to a single exponential fit (red, dotted). The most notable difference between spinor and SR electron cooling is the ~1.5 orders of magnitude difference in cooling to LU state. This can be attributed to large SOC experienced by Pb-6p states near conduction band edge which reduces the DOS.

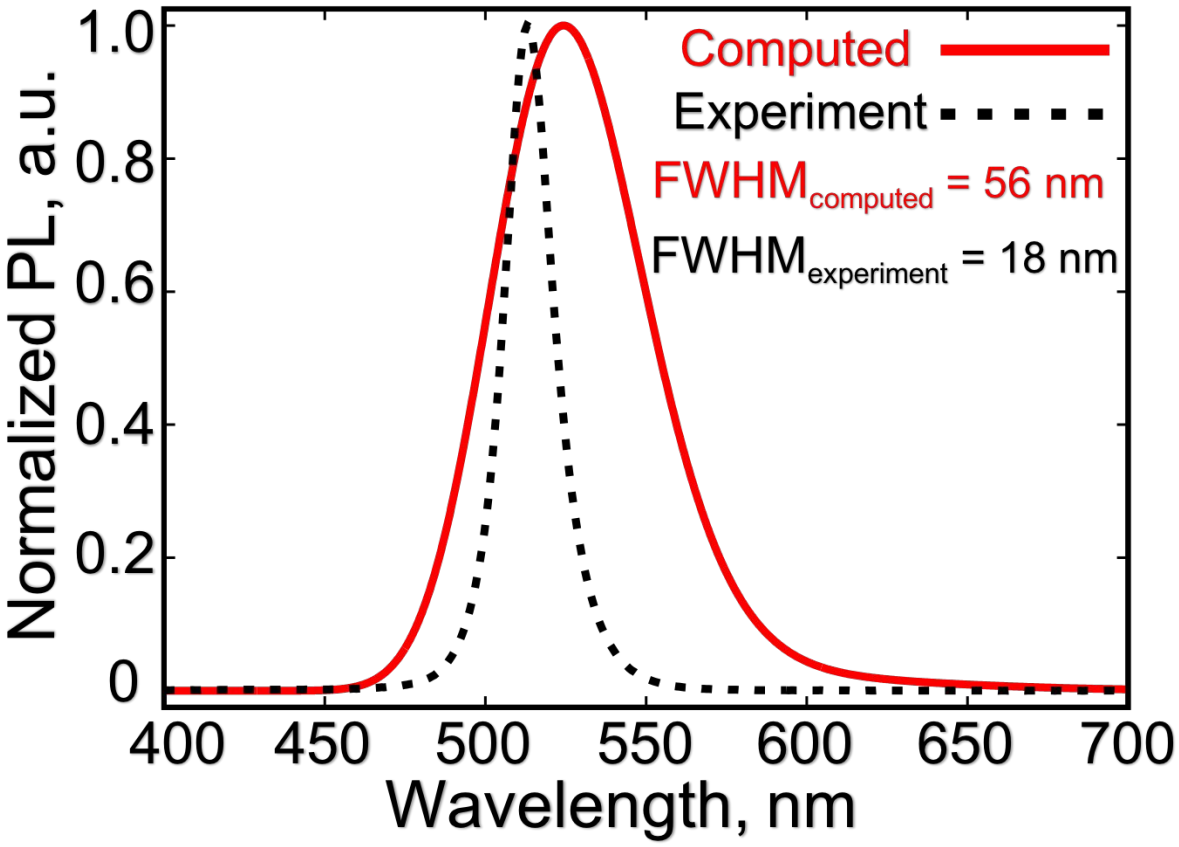

SI Figure S8: Comparing experimental PL linewidths (black, dotted) of $CsPbBr_3$ NCs to computed line widths using MDPL protocol described in main text using SKSO basis (red, solid). The full-width-at-half-max (FWHM) for experimental and computed model is 18 nm and 56 nm, respectively.

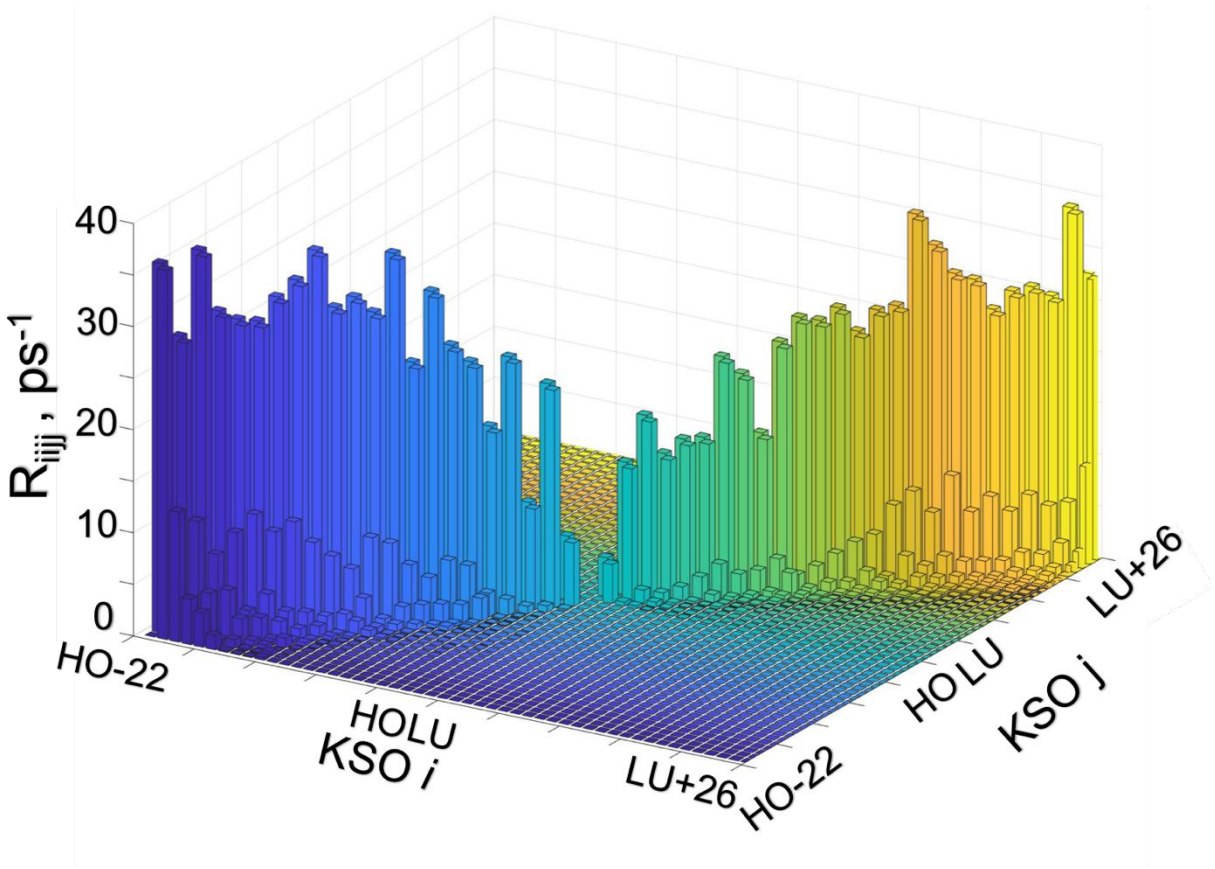

SI Figure S9: Redfield tensor $R_{ii,jj}$ computed using (SR) methodology within an orbital window of HO-22 to LU+26. It is observed that the majority of transitions are located between adjacent states $R_{i-1,i-1,jj}$ with few transitions $R_{i-x,i-x,jj}$ where $x < 3$. Compared to the Redfield tensor computed using non-collinear basis with SOC in **Figure 2(b)** it is seen there are fewer transitions above a threshold of 1 ps^{-1} (see **SI Figure S4 (a)-(b)).**

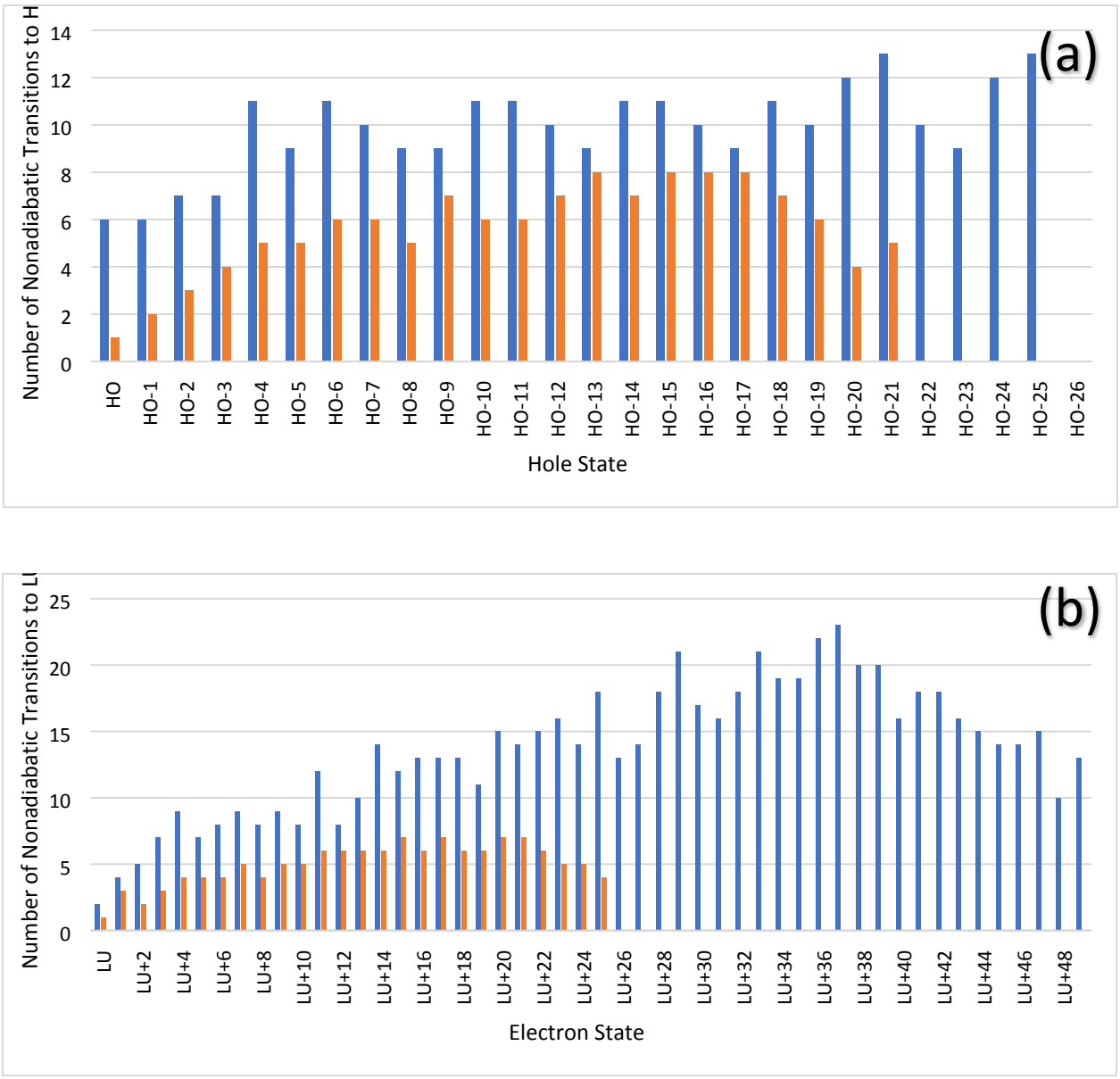

SI Figure S10: Histogram displaying the number of state-to-state transitions to state **(a)** HO-x and **(b)** LU+y with a rate above 1 ps^{-1} using SKSO (blue) and SR (orange) basis.

k_{rad} [1/ns]	Temperature	Source
1.86	0 K	Table 1(main manuscript)
0.96	300 K	Table 2(main manuscript)
2.63	5 K	[3]Efros et. al.
0.18	273 K	[4]Alivisatos et. al.

SI Table S4: Here we compare k_{rad} of $CsPbBr_3$ NCs computed from optimized geometry (0 K) and averaged over the MD trajectory (300K) to reported experimental values at analogous temperatures. We note that Table 1 shows the oscillator strength f_{ij} and transition energy E_{trans} used to compute the corresponding k_{rad}. It is observed that the same temperature dependent trend occurs in both computed values and experimental values, with k_{rad} decreasing with increasing temperature. This is in contrast to chalcogenide NCs where the opposite trend is observed due to the lowest energy interband transition being dark.

References

1. Protesescu, L.; Yakunin, S.; Bodnarchuk, M. I.; Krieg, F.; Caputo, R.; Hendon, C. H.; Yang, R. X.; Walsh, A.; Kovalenko, M. V., Nanocrystals of Cesium Lead Halide Perovskites (CsPbX(3), X = Cl, Br, and I): Novel Optoelectronic Materials Showing Bright Emission with Wide Color Gamut. *Nano Lett.* **2015,** *15*, 3692-6.
2. Bulik, I. W.; Scalmani, G.; Frisch, M. J., Noncollinear Density Functional Theory having Proper Invariance and Local Torque Properties. *Phys. Rev. B* **2013,** *87*, 035117.
3. Becker, M. A.; Vaxenburg, R.; Nedelcu, G.; Sercel, P. C.; Shabaev, A.; Mehl, M. J.; Michopoulos, J. G.; Lambrakos, S. G.; Bernstein, N.; Lyons, J. L.; Stöferle, T.; Mahrt, R. F.; Kovalenko, M. V.; Norris, D. J.; Rainò, G.; Efros, A. L., Bright Triplet Excitons in Caesium Lead Halide Perovskites. *Nature* **2018,** *553*, 189.
4. Koscher, B. A.; Swabeck, J. K.; Bronstein, N. D.; Alivisatos, A. P., Essentially Trap-Free CsPbBr3 Colloidal Nanocrystals by Postsynthetic Thiocyanate Surface Treatment. *J. Am. Chem. Soc.* **2017,** *139*, 6566-6569.